



UNIVERSITY OF LEEDS

This is a repository copy of *Sulfuric acid degradation of alkali-activated metakaolin cements supplemented with brucite*.

White Rose Research Online URL for this paper:
<https://eprints.whiterose.ac.uk/174506/>

Version: Accepted Version

Article:

Gevaudan, JP, Craun, Z and Srubar III, WV (2021) Sulfuric acid degradation of alkali-activated metakaolin cements supplemented with brucite. *Cement and Concrete Composites*, 121. 104063. ISSN 0958-9465

<https://doi.org/10.1016/j.cemconcomp.2021.104063>

© 2021, Elsevier. This manuscript version is made available under the CC-BY-NC-ND 4.0 license <http://creativecommons.org/licenses/by-nc-nd/4.0/>.

Reuse

This article is distributed under the terms of the Creative Commons Attribution-NonCommercial-NoDerivs (CC BY-NC-ND) licence. This licence only allows you to download this work and share it with others as long as you credit the authors, but you can't change the article in any way or use it commercially. More information and the full terms of the licence here: <https://creativecommons.org/licenses/>

Takedown

If you consider content in White Rose Research Online to be in breach of UK law, please notify us by emailing eprints@whiterose.ac.uk including the URL of the record and the reason for the withdrawal request.



eprints@whiterose.ac.uk
<https://eprints.whiterose.ac.uk/>

1 **Acid Attack of Alkali-Activated Metakaolin Cements Supplemented with Brucite**
2 **as a Mineral Admixture**

3 *Juan Pablo Gevaudan¹, Zoey Craun¹, Wil V. Srubar III^{1,2,†}*

4 ¹Department of Civil, Environmental, and Architectural Engineering, University of Colorado
5 Boulder, Boulder, Colorado USA. ²Materials Science and Engineering Program, University of
6 Colorado Boulder, Boulder, Colorado USA. [†]Corresponding Author 1111 Engineering Drive,
7 ECOT 441 UCB 428, Boulder, Colorado USA 80309. T +1 303 492 2621, E:

8 wsrubar@colorado.edu
9

10 **Abstract**

11 This study investigated the effect of alkali content (Na:Al = 0.86 and 1.39) and brucite (*i.e.*,
12 Mg(OH)₂) mineral addition on the sulfuric acid resistance of alkali-activated metakaolin (*i.e.*,
13 geopolymers). Geopolymers consist primarily of a sodium-stabilized aluminosilicate hydrate (N-
14 A-S-H) framework. Results demonstrate that higher alkali contents and brucite addition
15 improves the acid resistance of N-A-S-H, as evidenced by reduced dealumination and Si and Na
16 leaching upon exposure to acid. These results are mechanistically explained by increased
17 retention of Mg⁺² within the microstructure and increased Mg-Al interaction upon acid exposure.
18 Higher Mg⁺² retention and increased Mg-Al coupling together provide empirical evidence of
19 *polyvalent cationic stabilization*—a mechanism involving polyvalent cations (*e.g.*, Mg⁺²) that
20 stabilize the N-A-S-H binder by arresting acid-induced electrophilic attack. Results further
21 illustrate that brucite addition, especially at high-alkali content formulations, reduces micro-scale
22 porosity while increasing the proportion of gel pores (< 5nm), which suggests that increased

23 tortuosity of gel pores may aid in Mg^{+2} retention and promote the increased Mg-Al coupling
24 observed herein.

25

26 **Keywords:** Alkali-activated materials, geopolymers, acid attack, mineral admixtures, pore
27 structure

28 **1. Introduction**

29 Calcium-free (Ca-free) alkali-activated cements (AACs), also named geopolymers, are primarily
30 composed of sodium-stabilized aluminosilicate hydrate (N-A-S-H) gels. These cementitious
31 binders can offer multiple benefits in terms of low- CO_2 emissions and durability properties
32 compared to portland cement [1–3]. Alkali-activation of an aluminosilicate material (*e.g.*,
33 metakaolin) begins with precursor dissolution in a high-pH activator solution, which releases
34 silica and alumina species [4]. As the precursor dissolves, silicate and alumina species
35 polymerize to form a cation-stabilized cementitious binder [5]. In Ca-free AACs, the main binder
36 comprises an amorphous N-A-S-H cementitious binder [6]. Lower Ca contents of N-A-S-H
37 materials have been linked to improved durability performance, namely for sulfate and seawater
38 attack, acid exposure, alkali-silica reaction, steel corrosion, and fire [7].

39 Biogenic acid corrosion of concrete structures is a major cause of civil infrastructure
40 deterioration. Corrosion due to sulfuric acid is the most common form of this mechanism [8].
41 Previous studies have shown that AACs are more resistant to acid attack than ordinary portland
42 cement (OPC) [9] [10]. Briefly, the acid degradation of calcium-free AACs begins with an ion-
43 exchange between framework cations (*i.e.*, sodium) and protons from the acid solution. The
44 protons induce an electrophilic attack, which results in the ejection of aluminum (*i.e.*,
45 dealumination) from the Si-O-Al bonds of the binder [11].

46 The complex mechanisms of acid deterioration of Ca-free AACs are not well understood.
47 Further research is needed to be able to better predict dissolution-precipitation reactions of the
48 AAC binders, while taking into consideration different factors, such as Si:Al ratios and varying
49 H₂O and cation contents [12]. In addition, more research is required to understand how mineral
50 phases—either unreacted minerals or minerals precipitated during alkali activation—affect acid
51 degradation [13–15]. The availability of network-modifying cations, such as magnesium (*i.e.*,
52 Mg⁺²), can affect the durability of AACs by influencing microstructural changes occurring
53 within the N-A-S-H gel either (1) during alkali activation or (2) upon exposure to acid. Previous
54 research has shown that minerals can provide multivalent cations, like Mg⁺², have the potential
55 to improve the acid resistance of AACs by stabilizing the gel at the acid degradation front
56 [16,17]. However, the chemical heterogeneity, polycrystallinity, and variability of many
57 industrial aluminosilicates that are used as precursors for alkali-activation (*e.g.*, slag, fly ash)
58 confound the mechanistic understanding of the role of Mg⁺² in acid degradation of AACs.

59 Brucite is a common mineral present in industrial aluminosilicate precursors used in the
60 production of AACs, such as high-magnesium and high-nickel slag and, to a lower extent,
61 natural clays (*e.g.*, bentonite). Brucite can also form as a result of alkali-activation, since it is
62 thermodynamically favorable to form under Al-deficient conditions that can exist during slag
63 activation [18–20]. Hence, due to its common presence in AACs and its solubility at low pH (*i.e.*,
64 acidic) conditions, it is important to understand the effect of brucite—and Mg⁺² specifically—on
65 the acid resistance of AACs. In this study, metakaolin was selected as the aluminosilicate
66 precursor due to the purity of its aluminosilicate chemical composition, high reactivity, and
67 proven ability to form N-A-S-H. By utilizing metakaolin, we consequently aim to isolate the role
68 of Mg⁺² during acid degradation of Ca-free AACs.

90 2. Materials and Experimental Methods

91 2.1 Materials

92 Metakaolin (MK) (MetaMax) was supplied by BASF Chemical Corporation (Georgia, USA).

93 The chemical composition of MK, as determined by ICP-OES, is shown in **Table 1**. ICP-OES

94 analysis was performed following the methodology reported in [21]. The alkali-activating

95 solution used was prepared using sodium hydroxide (Sigma-Aldrich, NaOH \geq 97%) and sodium

96 silicate (Sigma-Aldrich, SiO₂ = 27 wt. %, Na₂O = 11 wt. %). Light metal (*i.e.*, Mg) addition to

97 the AACs was provided in the form of brucite powder (Sigma-Aldrich, Mg(OH)₂ \geq 95%). After

98 the AAC pastes were created, the samples were exposed to a sulfuric acid solution with a pH of

99 2.0 ± 0.07 . The sulfuric acid solutions were prepared by adding concentrated sulfuric acid

100 (Sigma-Aldrich, H₂SO₄ \geq 95%) to deionized water.

101 **Table 1**, Chemical composition of metakaolin in weight percentage (wt. %).

(wt.%)	SiO ₂	Al ₂ O ₃	CaO	SO ₄	Fe ₂ O ₃	K ₂ O	Na ₂ O	P ₂ O ₅
Metakaolin	54%	47%	0.10%	0.30%	0.40%	0.10%	0.30%	0.10%

102

103 2.2 Experimental methods

104 The experiments were designed using a 2² factorial design of experiments. Specific proportions

105 and constituent materials for each mixture design formulation (see **Table 2**) were selected based

106 on ranges explored in previous studies. To enable the explicit study of MK-activated

107 formulations that form faujasite minerals, the alkali (*i.e.*, sodium, Na⁺) to aluminum ratio (Na:Al)

108 was varied to produce cements with Na:Al ratios of 0.86 and 1.39. As previously elucidated by

109 the authors in [21], Na:Al ratios of 1.39 and Si:Al ratios of 1.15 form faujasite minerals, while

110 lower Na:Al ratios of 0.86 do not exhibit these mineral dynamics. Samples were prepared

Deleted:

132 without and with the addition of brucite to explore the effect of these magnesium mineral on acid
 133 degradation of alkali-activated MK materials. In order to meet these Na:Al ratios and produce N-
 134 A-S-H binders during alkali-activation of MK the mass amounts of MK and alkali-activator
 135 solutions were not increased with brucite supplementation – a chemically inert mineral
 136 admixture during alkali-activation. However, it is important to note that the low liquid-to-solid
 137 ratio of brucite-supplemented samples resulted poor workability and, as reported in [22] , present
 138 less effective dispersion of raw materials. Workability issues were circumvented by employing
 139 high-shear mixing of all samples, as detailed in section 2.3. Brucite was added to obtain a Mg:Si
 140 ratio of 0.85, which was chosen based on previous research related to the synthesis of
 141 magnesium silicate hydrate (M-S-H) gels [23][16]. Such a high ratio studied herein result in a
 142 fundamental investigation of Mg chemical modification of the N-A-S-H binders present in
 143 alkali-activated MK materials.

144 **Table 2.** Mixture proportions for metakaolin-based alkali-activated cement control and Mg(OH)₂
 145 addition samples.

Sample ID		Constituent Materials				Important Parameters		
Sample Name	MK (g)	Mg(OH) ₂ (g)	NaSi (mL)	NaOH (g)	H ₂ O (ml)	Mg:Si	Si:Al	Na:Al
MK Control Low	50	0	13.5	13	45	0	1.15	0.86
MK Control High	50	0	13.5	22.8	45	0	1.15	1.39
Control Low + Mg	50	26.4	13.5	13	45	0.85	1.15	0.86
Control High + Mg	50	26.4	13.5	22.8	45	0.85	1.15	1.39

146
 147 *2.2.1 AAC sample preparation*

148 AAC pastes were prepared using the calculated amounts of metakaolin, sodium silicate, sodium
 149 hydroxide, deionized water, and brucite (Mg(OH)₂) shown in [Such a high ratio studied herein](#)
 150 [result in a fundamental investigation of Mg chemical modification of the N-A-S-H binders](#)
 151 [present in alkali-activated MK materials.](#)

Formatted

174 **Table 2.** These components were mechanically mixed in a high-shear mixer for 3 minutes before
175 being cast in molds (diameter 2.5 – 2.7 cm), after which the mixtures were tamped for 30
176 seconds and vibrated for 30 seconds. Paste samples were then cured in sealed containers (99%
177 RH) in a Quincy forced air laboratory oven for 48 hours (2 days) at 40 °C. After initial curing,
178 samples were demolded and cured 35 ± 5 °C for an additional 24 hours (1 day). These curing
179 periods were selected to control the mineral dynamics of metakaolin-based alkali-activated
180 materials (i.e., extent of formation of faujasite minerals in MK control High and Control High +
181 Mg samples) [21].

182 *2.2.2 Acid exposure and leaching*

183 Samples were exposed to a sulfuric acid solution (pH 2.0 ± 0.07) twice until pH equilibrium was
184 attained, defined as $\Delta\text{pH} < 0.0025$ per hour. A modified ASTM C1308 methodology was
185 employed to expose samples to acid. Modifications consisted of a volume-to-surface-area ratio
186 of seven to determine the amount of acid solution to be used for each exposure as well as
187 collection of the leachate only after pH equilibrium was attained. This pH-driven data collection
188 ensures that information from complete acid-base reactions is collected and analyzed. Samples
189 were suspended using a 46 mm Savillex support screen (730-0046) and stirred continuously in an
190 acid solution using a magnetic stirrer to ensure homogenous solution mixing. Triplicates were
191 utilized to ensure statistical robustness of the data. After pH equilibrium, leachate samples were
192 collected, and acid solutions were replaced. Leachate samples were analyzed *via* ICP-OES and
193 ICP-MS. To account for brucite supplement by mass, the leaching data were normalized by the
194 surface area of the cylindrical samples and cement content so to facilitate comparison between
195 samples.

197 2.2.3 *Mineralogical characterization*

198 Mineralogy was determined *via* semi-quantitative X-ray diffraction (XRD) using Cu K α
199 radiation (Siemens D500 X-ray diffractometer). An internal standard (*i.e.*, corundum, American
200 Elements) was employed to normalize peak heights between samples and align diffraction
201 patterns. Samples were homogenized by creating fine powders using a micronizing mill with
202 well-packed yttrium-stabilized zirconium grinding beads. Subsequently, samples were
203 homogenized in a plastic scintillation vial with three Delrin balls. 500 μ L of Vertrel cleaning
204 agent (Miller-Stephenson) was added to randomize particle orientation *via* the formation of
205 aggregates. Lastly, samples were sieved through a 250 μ m mesh and packed into XRD analysis
206 plates. Samples were then analyzed from 5 to 65 degrees 2θ using Cu K α X-ray radiation, with a
207 step size of 0.02 degrees and a dwell time of 2 seconds per step. Diffraction patterns were
208 analyzed using Jade software (MDI, Version 9) and the International Centre for Diffraction Data
209 (ICDD) 2003 database.

210 2.2.4 *Microstructural Mg:Al ratio determination*

211 Electron microprobe analysis was employed using a JEOL JXA-8230 electron probe
212 microanalyzer outfitted with five wavelength-dispersive spectrometers (WDS) and a
213 Thermoscientific energy dispersive spectrometer (EDS) to examine the chemical composition of
214 the AAC microstructure, namely changes in Mg:Al ratio upon acid exposure. The acceleration
215 voltage and beam current used for all WDS acquisition was 15keV and 100nA, respectively. The
216 pixel size chosen was 6 μ m, and the electron beam was adjusted to match the size. Lastly, a
217 dwell time of 20 msec was used. The data were processed using CalcImage software
218 (ProbeSoftware, Inc.) in order to apply the mean atomic number (MAN) background correction.
219 EDS acquisition was standard-less using a spectral acquisition of 15 seconds, which was

220 sufficient to accumulate counts over 4000. An acceleration voltage of 15 keV and a beam current
221 of 20 nA was used for all acquisitions. An elemental matrix correction (ZAF) was performed in
222 all acquisitions. Twenty randomized points were collected for five different locations in all
223 samples (top, bottom, center, left, and right), totaling an acquisition of 100 EDS points per
224 sample.

225 *2.2.5 Nano- and micro-scale porosity determination*

226 Nitrogen (N₂) adsorption using a Gemini V apparatus (Micromeritics) was used to characterize
227 nano-scale gel porosity of unexposed and acid-exposed AAC samples. Identical sample
228 formulations as those detailed in **Table 2** were prepared with unique sample sizes to fit test tubes
229 (diameter: 0.65 cm, height: 1.4 cm) needed for N₂ adsorption experiments. Hence, materials were
230 tested as a whole. All materials were first degassed for 24 hours in a vacuum (< 100 mTorr). For
231 specific samples, duplicate measurements were collected. Porosities and pore-size distributions
232 were calculated using the Barrett-Joyner-Hallenda (BJH) method prior to sulfuric acid exposure.
233 Later, in order to characterize the unexposed micro-scale porosity, whole samples were subjected
234 to X-ray micro-computed tomography (μ -CT) analysis in a Zeiss Xradia 520. Samples were
235 secured in commercial plastic vials (diameter: 2.5 cm) and scanned using a 0.4x objective and X-
236 ray source parameters of 60 kV acceleration voltage and 4 Watts. An air filter was utilized to
237 reduce the transmission values between 29% and 60% and maintain intensity counts above 5000
238 by regulating the exposure time. A pixel size resolution of 5.786 microns was achieved utilizing
239 a bin 1 pixel averaging acquisition.

240 Once the initial pore structure was characterized, samples were exposed to sulfuric acid
241 as detailed in section 2.2.2. The acid-attacked micro-scale pore structure was subsequently
242 characterized by μ -CT scans with the same settings as those stated previously. After μ -CT

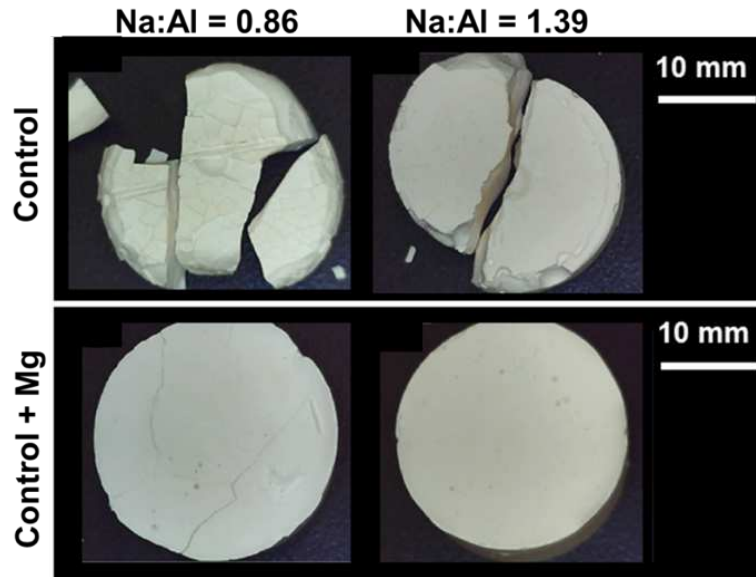
243 scanning, the N₂ adsorption experiments employing the BJH method was conducted to
244 characterize the impact of acid exposure on the sample's nanoscale pore structure, as detailed
245 above. This procedure enabled the investigation of acid effects on both nano- and micro-scale
246 porosity for the whole sample, including both affected and unaffected areas.

247 All μ -CT scans were reconstructed using the ZEISS Scout-and-Scan Control System
248 Reconstructor (V.11.1.6411.17883) software to manually adjust the center shift values and
249 minimize beam hardening artifacts. Prior to pore-structure segmentation, image pre-processing in
250 Dragonfly 4.0 was required to minimize noise from acidic solutions. Denoising and smoothing
251 were performed utilizing an Open mathematical morphology operation (circle kernel size of 7), a
252 median smoothing (circle kernel size of 3), and a non-local means smoothing (square kernel size
253 of 9). Such a procedure enabled consistent segmentation across all scans.

254 **3. Results and Analysis**

255 **3.1 Physical Evidence of Sulfuric Acid Degradation**

256 The addition of brucite visibly improved the pH ~2 acid resistance of the AAC formulations
257 investigated herein, as visually demonstrated in **Figure 1**. Failure of control formulations without
258 brucite addition was evident at both alkali contents, indicating a greater extent of binder
259 breakdown by sulfuric acid attack in those samples. While structural integrity was maintained in
260 Control Low + Mg samples, shallow surface cracks were observed, indicating some surface-level
261 degradation. However, Control High + Mg samples maintained structural integrity and exhibited
262 no observable cracking, suggesting that brucite addition improved the sulfuric acid resistance of
263 the high-alkali sample.



264

265 **Figure 1.** Visual evidence of a sulfuric acid attack on Ca-free AACs for representative non-
 266 supplemented samples (control) and supplemented samples with brucite (control + Mg).

267

268 3.2 Chemical Evidence of Sulfuric Acid Degradation

269 Brucite addition increased elemental silicon (Si) retention upon acid exposure, as demonstrated
 270 by a reduced loss (*i.e.*, reduced leaching) of Si (see **Table 3**). Low Na:Al samples with brucite
 271 revealed negligible differences during the first acid exposure but a 75% decrease during the
 272 second acid exposure. Incorporation of brucite in higher Na:Al content formulations (Control
 273 High samples) decreased Si leaching 35% and 75% of during the first and second acid exposure
 274 cycles, respectively. However, the concentration of leached Si remained high in these
 275 formulations and is observed to correlate well with sodium (Na) leaching. This result can be
 276 explained by the presumed existence of Si monomers and dimers in the pore solution, which can
 277 polymerize and gelate *via* Na^{+1} stabilization. Recent studies of Na:Al = 1.0 AACs have found an
 278 increased content of orthosilicic acid (*i.e.*, Si monomers) 15 hours after alkali-activation [24,25].

279 This increase in monomeric Si concentration enables the formation of silica gel networks within
 280 the perimeter of the sample—a well-known phenomenon of AACs [2,11,26,27].

281 The addition of brucite improved the acid resistance of AACs by reducing dealumination
 282 of the Si-O-Al bonds in the N-A-S-H binder. Upon first acid exposure, regardless of brucite
 283 addition or alkali content, dealumination and magnesium (Mg) leaching is minimal for both
 284 formulations that contain Mg (**Table 3**). However, upon second acid exposure, dealumination
 285 increased in samples without brucite. Increased dealumination occurs concomitantly with a
 286 decrease in Na leaching, indicating that the electrophilic attack of protons cannot be arrested
 287 solely by the alkalinity within the AAC. Contrastingly, samples containing brucite release Mg,
 288 indicating that the dissolution of brucite aids in increasing the alkalinity (*i.e.*, pH buffering
 289 capacity) of these formulations. High Na:Al samples with brucite are observed to retain
 290 dissolved Mg and simultaneously exhibit lower dealumination. These results chemically support
 291 the physical evidence observed in **Figure 1** that brucite improves the acid resistance of AACs,
 292 especially at high alkali contents.

293

294 **Table 3.** Normalized elemental leaching for all samples for both first and second acid exposure
 295 after achieving pH equilibrium.

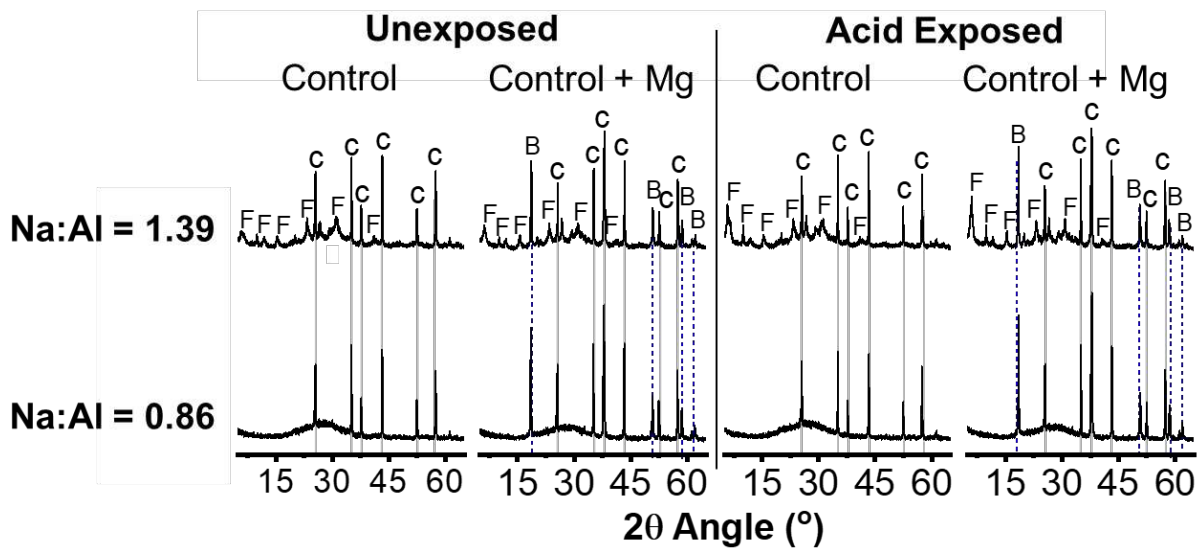
	1st Equilibrium							
	MK Control Low		Control Low + Mg		MK Control High		Control High + Mg	
	<i>mean</i>	<i>s.d.</i>	<i>mean</i>	<i>s.d.</i>	<i>mean</i>	<i>s.d.</i>	<i>mean</i>	<i>s.d.</i>
Si	0.05	0.007	0.05	0.004	1.61	0.034	0.96	0.068
Al	0.16	0.010	0.03	0.002	0.04	0.005	0.04	0.014
Na	7.96	0.135	6.45	1.505	15.02	0.422	12.87	2.776
Mg	-	-	0.02	0.006	-	-	0.00	0.001

2nd Equilibrium

	MK Control Low		Control Low + Mg		MK Control High		Control High + Mg	
	<i>mean</i>	<i>s.d.</i>	<i>mean</i>	<i>s.d.</i>	<i>mean</i>	<i>s.d.</i>	<i>mean</i>	<i>s.d.</i>
Si	0.45	0.037	0.16	0.037	0.44	0.003	0.13	0.006
Al	0.06	0.054	0.00	0.000	0.05	0.039	0.00	0.000
Na	2.11	0.236	2.38	0.386	2.16	0.109	2.95	0.426
Mg	-	-	0.30	0.055	-	-	0.03	0.020

296

297 Mineralogies of Control and Control + Mg samples before and after acid exposure remain
298 unchanged between formulations (see **Figure 2**), indicating that no significant precipitation
299 reactions occurred during acid exposure. All samples indicate a predominantly amorphous
300 component, identified by a hump $\sim 25^\circ$ 2θ angles. This amorphous component is indicative of N-
301 A-S-H. Silicon-rich faujasite minerals ($\text{Na}_{2.06}\text{Al}_2\text{Si}_{3.8}\text{O}_{11.63}\cdot 8\text{H}$) form in high sodium content
302 ($\text{Na}:\text{Al} = 1.39$) formulations, regardless of brucite addition, as expected [21]. Upon acid
303 exposure, minimal changes in the mineralogy of AACs are observed. High $\text{Na}:\text{Al}$ samples
304 demonstrated an increased diffraction intensity of faujasite after acid exposure, possibly
305 indicating further mineralization during acid exposure. Similar mineralization reactions after
306 acidic exposure observed by [28] were also correlated to reduced porosity and increased
307 mechanical performance. Thus, these results indicate that acid degradation of these Ca-free
308 AACs does not involve significant precipitation reactions as observable in Ca-rich cementitious
309 materials, which form gypsum (*e.g.*, $\text{CaSO}_4\cdot 2\text{H}_2\text{O}$) phases upon exposure to sulfuric acid
310 [29,30].



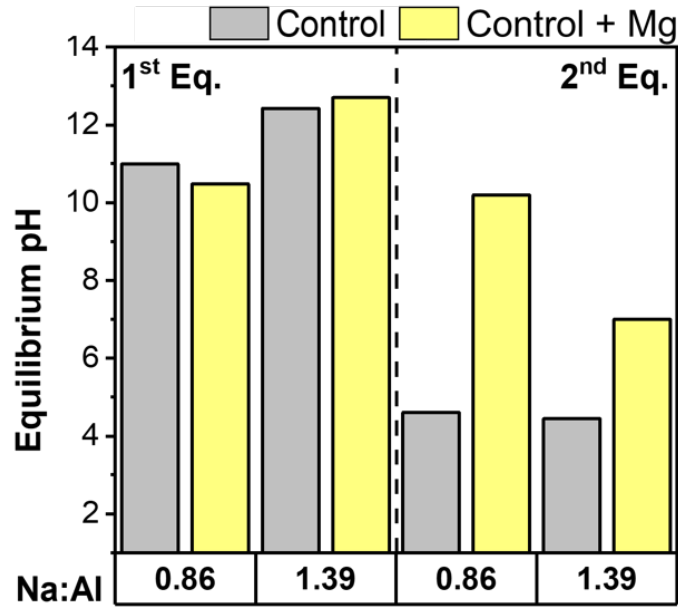
311
 312 **Figure 2.** Mineralogy of AAC samples without and with brucite before and after acid exposure.
 313 Symbols correspond to mineral phases identified as follows: “F” indicates the presence of
 314 faujasite-Na ($\text{Na}_{2.06}\text{Al}_2\text{Si}_{3.8}\text{O}_{11.63}\cdot 8\text{H}_2\text{O}$); “B” indicates the presence of brucite ($\text{Mg}(\text{OH})_2$); and,
 315 “C” indicates the presence of corundum (Al_2O_3), which was used as an internal standard.

316 The acid neutralization capacity of AACs increases with the addition of brucite during
 317 the second acid exposure (**Figure 3**). Brucite-supplemented samples attained a higher
 318 equilibrium pH values indicating a higher acid neutralization capacity than their control
 319 counterparts. During the first acid exposure, regardless of alkali content, equilibrium pH values
 320 of all samples are not statistically different (p-value of 0.517). As discussed earlier in regard to
 321 leaching data (**Table 3**), pH values are highly correlated with an increase in Na^+ leaching during
 322 the first acid exposure. The correlation was verified by computing the Pearson correlation
 323 coefficient, which yielded a value of 0.938 (p-value of 0.0001). This correlation is expected,
 324 given that an inter-cationic exchange between H^+ and Na^+ occurs during the first step of acid
 325 degradation of N-A-S-H. Also, the acid-base reaction of trace carbonates and hydroxides in the

326 pore solution (e.g., Na₂CO₃, NaOH) may contribute to this leaching correlation. However, the
327 presence of these phases in the pore solution is speculated as XRD was unable to resolve distinct
328 patterns in the solid phase of these materials (**Figure 2**). Remnant NaOH is evidenced by high
329 equilibrium pH values (*i.e.*, 12.4, 12.7) attained in high Na-content formulations (Na:Al = 1.39).
330 However, during the second acid exposure, samples without brucite demonstrated a low acid
331 neutralization capacity, achieving equilibrium pH < 4.6. The addition of brucite improves acid
332 neutralization capacity. Control Low + Mg and Control High + Mg samples reach pH values of
333 10.2 and 7.0, respectively, during the second acid exposure.

334 It is worth noting that, while Control High + Mg samples attain lower pH equilibrium
335 conditions, these samples simultaneously demonstrate high Mg retention (**Figure 2**), which
336 indicate differences in acid-base reactions occurring in the samples. In order to explain the
337 differences in the acid-base reactions occurring in the pastes, a microstructural chemical analysis
338 was performed. More specifically, Mg:Al ratios of the pastes were determined before and after
339 exposure to acid. While Control Low + Mg formulations exhibited higher acid neutralization
340 capacity, Control High + Mg samples were evidently more acid resistant.

341 The high Na:Al samples with brucite exhibit a two-fold increase in Mg:Al ratio within
342 their microstructures after the second acid exposure (**Figure 4**). The increase of Mg and Al
343 spatial pairing is likely a result of Mg stabilization of negative moieties along with the acid-
344 attacked Si-O-Al bonds – a process name *polyvalent cationic stabilization* and previously
345 hypothesized in [17]. Contrastingly, Control Low + Mg samples demonstrate lower Mg:Al ratios
346 after acid exposure a consequence of high Mg leaching (**Table 3**). This observed leaching of
347 alkalis (e.g., Na, Mg, K, Ca) is a common phenomenon that has been previously observed in
348 AACs [31–33].



349

350 **Figure 3.** Equilibrium pH of sulfuric acid solutions for samples without and with brucite. Data
 351 show pH of the leachate after the first and second acid equilibrium exposure cycles.

352 Polyvalent cationic stabilization of negative moieties in the N-A-S-H binder can occur
 353 due to functionalized brucite surfaces or release of Mg^{+2} cations. Seminal research on Brucite
 354 ($Mg(OH)_2$) surface chemistry has shown that the protonation of the mineral surface ($>Mg-OH$)
 355 yields $>MgOH_2^+$ sites, which are at a maximum concentration on brucite surfaces at pH values <
 356 7.0. As observed in **Figure 3**, the final equilibrium pH of Control High + Mg samples is 7.0,
 357 which may enable dipole-dipole interactions between $>MgOH_2^+$ and negative moieties of the
 358 surrounding N-A-S-H binder [34]. Additionally, $>MgOH_2^+$ surface sites also enable the
 359 dissolution and release of Mg^{+2} ions, according to the thermodynamically preferred dissolution
 360 reaction (pike -16.844) [35,36]:

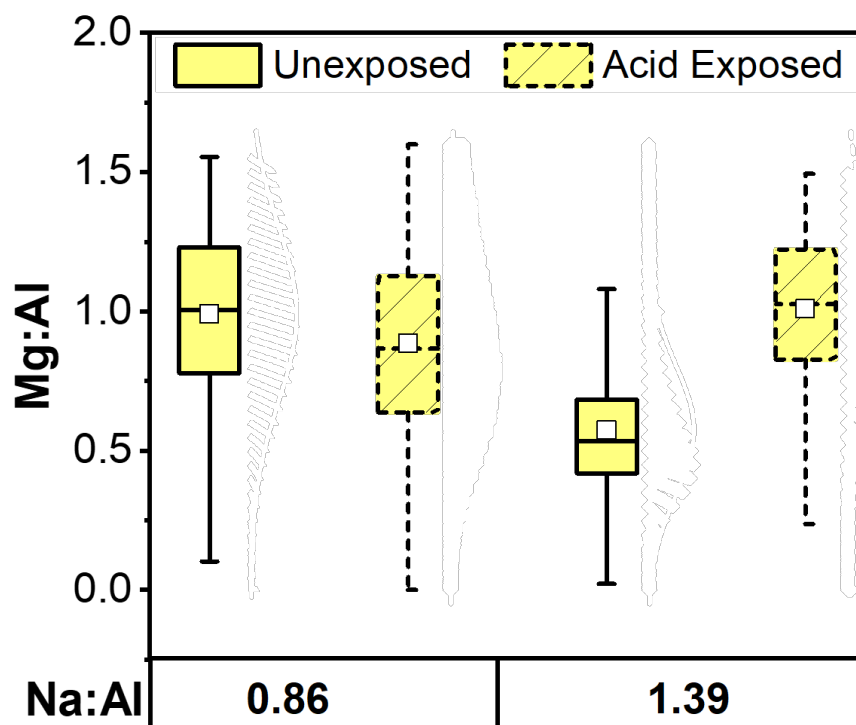
361



363 Eq. 1

364

365 Lastly, the small atomic radii of Mg^{+2} ions are advantageous in terms of its mobility, which
366 would facilitate leaching. However, results presented here suggest a higher retention of Mg^{+2} due
367 to Mg-Al interactions in the high Na:Al samples with brucite. Thus, it is evident that a higher
368 number of Mg-Al interactions within the AAC microstructure yield improved acid resistance
369 with a lower breakdown of the Si-O-Al bonds of N-A-S-H binders



370

371 **Figure 4.** Distribution and mean atomic Mg:Al ratio of Control Low + Mg (Na:Al = 0.86) and
372 Control High + Mg (Na:Al = 1.39) AAC samples before and after acid exposure.

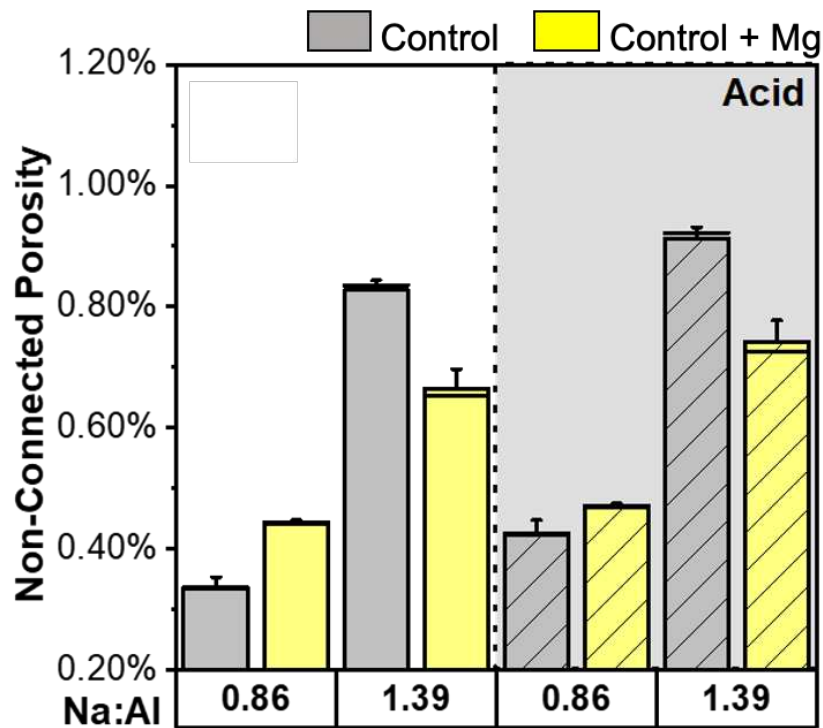
373 3.3 Porosity of Alkali-Activated Cements Supplemented with Brucite

374 Micro-scale porosities of all samples before and after acid exposure are shown in **Figure 5**. Non-
375 connected porosities between 0.3%-0.8% are comparable to those reported by X-ray

376 microtomography (μ CT) studies of other fly ash-based AACs [37,38]. Results in **Figure 5**

377 demonstrate that the addition of brucite at high Na:Al formulations decrease by 18% the porosity

378 of AACs, while the opposite effect is observed at low Na:Al formulations containing brucite
 379 demonstrating a 26% porosity increase.
 380 As observed in **Figure 5**, increased alkali-content results in higher porosity values as observed
 381 for Control High formulations. This is a dissimilar trend reported in other AAC literature, where
 382 increased Na content is expected to decrease porosity due to an increased formation of reaction
 383 products and a denser microstructure [39]. Observed porosity differences, although minor, may
 384 be explained by utilization of activating solutions with low silica modulus (M_s) values ($M_s =$
 385 0.27) at high Na:Al formulations [40]. These activating solutions have higher viscosities due to
 386 higher contents of dissolved Na and Si ions and, hence, an increase of porosity is anticipated as a
 387 consequence of entrapped air during mixing [41–43]. This likely results in decreased compressive
 388 strength, due to a lower bulk density associated with higher porosities in less workable mixes
 389 [44].

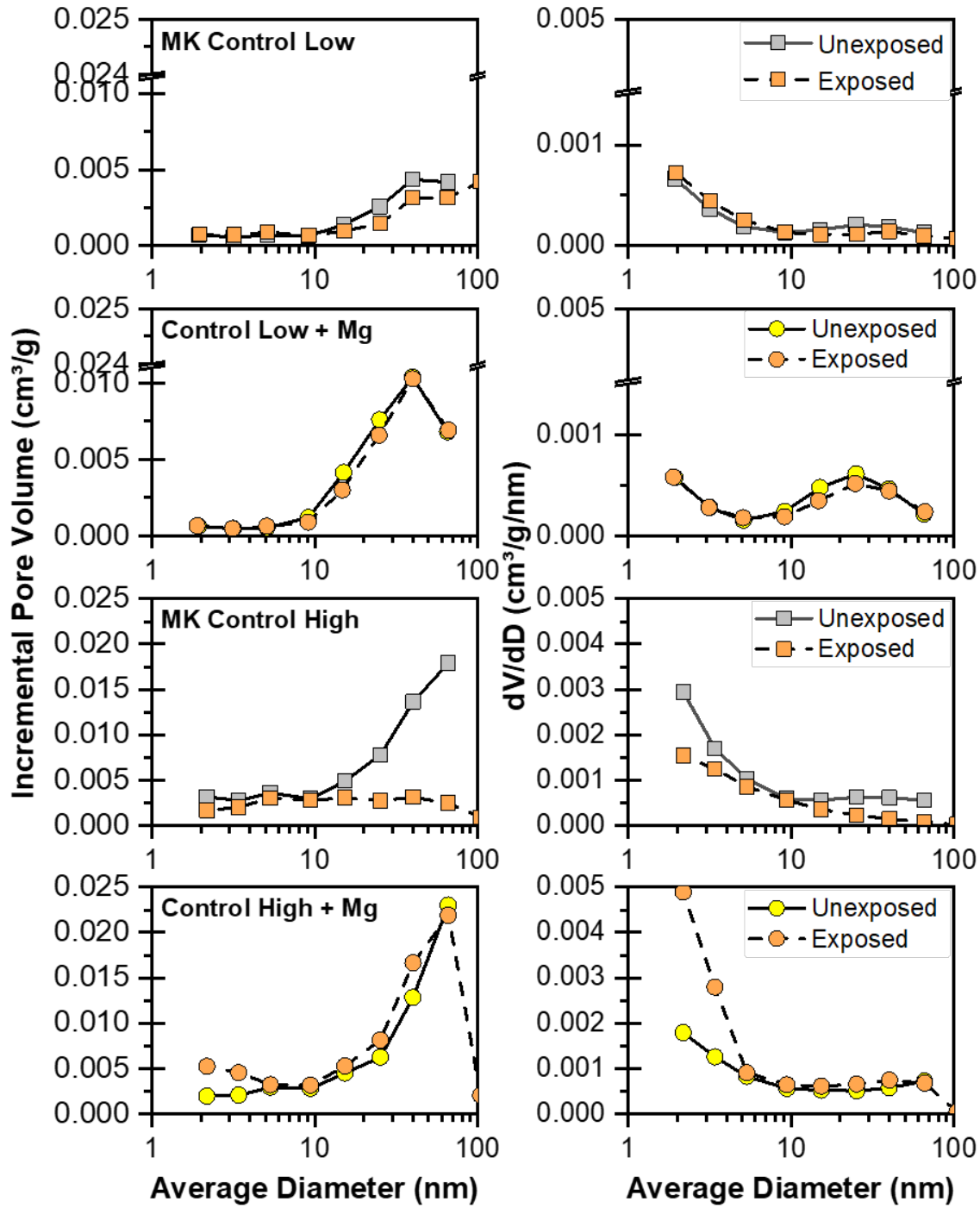


390

391 **Figure 5.** μ -CT non-connected porosities of all AAC samples before and after the first sulfuric
392 acid exposure (pH of 2.0 ± 0.07).

393 Regardless of brucite addition, AACs develop higher micro-scale porosities during the
394 first acid exposure. The addition of brucite reduces the increase in porosity for both Control Low
395 and Control High formulations by 50.9% and 14.1%, respectively. These results correlate well
396 with the lower Na and Si leaching of these samples (**Table 3**). The expected Si gelation and
397 retention of Na ions likely plays a role in decreasing the changes in porosity at the micro-scale of
398 brucite-supplemented AACs. Moreover, results suggest that the preservation of the pore structure
399 in Control Low + Mg samples correlates with reduced dealumination. In light of the Mg:Al
400 results shown in **Figure 4**, as well as leaching results presented in **Table 3**, Control High + Mg
401 samples may preserve their porous structure as a result of Mg-Al stabilization. The formation of
402 crystalline faujasite phases during acid attack, as discussed in **Figure 2**, may also play a role in
403 pore-structure preservation.

404 Addition of brucite in low Na:Al formulations is observed to double the gel pore volumes
405 above a pore size of 10 nm (**Figure 6**). In general, the opposite trend is observed at high Na:Al
406 formulations with brucite (Control High + Mg) as these samples exhibit a $\sim 30\%$ lower nano-
407 scale porosity when compared to samples without brucite. Moreover, when analyzing the effect
408 of alkali content, Control High formulations have a higher content of nano-scale porosity, when
409 compared to Control Low. These nano-scale porosity trends are consistent with the micro-scale
410 porosity trends observed in **Figure 5**. Increased micro- and nano-scale porosity at higher sodium
411 contents may be due to residual inter-layer porosity from unreacted MK precursor, as well as
412 rheology differences due to extent of binder network formation, as previously discussed [45].



413

414 **Figure 6.** Nano-scale porosity characterization of all samples without and with brucite addition

415 before acid exposure and after sulfuric acid exposure (pH of 2.0 ±0.07).

416

417 Upon acid exposure, there is an apparent decrease in incremental pore volume in samples
418 without brucite, see **Figure 6**. Given the utilization of BJH, the apparent decrease in nano-scale
419 pore volume may actually be a consequence of acidic dissolution, which may create larger pores
420 (> 100 nm) outside of the method's pore size range. This result is supported by a higher extent of
421 Si-O-Al breakdown as shown by high leaching of Na, Si, and Al (**Table 3**) as well as the
422 increased micro-scale porosity (**Figure 5**).

423 Nonetheless, it is evident that the addition of brucite preserves nano-scale porosity.
424 Interestingly, only Control High formulations with brucite double in nano-scale porosity (<
425 5nm), which may increase the tortuosity of porous network and, hence, increase the dissolution
426 of brucite. Similar observable increases in tortuosity have been reported in previous experiments
427 with chemically-active mineral admixtures [46]. As Mg^{+2} ions are liberated from the acid-
428 induced dissolution of brucite, the higher tortuosity may increase the probability of Mg^{+2}
429 encountering negative moieties along the acid-attack N-A-S-H binder. This phenomenon could
430 suggest a higher Mg retention (**Table 3**) and concomitant lower acid neutralization capacity
431 (**Figure 3**), which would lead to increased Mg-Al pairing within the microstructure (**Figure 4**).
432 Together, these results indicate that the increase in tortuosity caused by an increase in nano-scale
433 gel pores after acid exposure may be critical to the effectiveness of the polyvalent cationic
434 stabilization mechanism.

435 **4. Conclusions**

436 We studied the effect of brucite, a common mineral found in unreacted and reacted AAC
437 materials, on the sulfuric acid resistance of alkali-activated metakaolin. Converging lines of
438 evidence suggest that brucite improves acid resistance by (1) increasing acid neutralization
439 capacity and/or (2) polyvalent cationic stabilization, depending on AAC formulation.

440 Experimental data indicate that brucite increases acid resistance in AACs with low alkali
441 contents (Na:Al = 0.86) by increasing acid neutralization capacity alone. Low Na:Al AACs with
442 brucite exhibit a high acid neutralization capacity, with equilibrium pH values reaching >10 after
443 the first and second acid exposure. This neutralization, in turn, resulted in decreased loss of Al,
444 Si, and Na upon acid exposure, indicating a reduced breakdown of Si-O-Al. The decreased
445 leaching of Al, Si, and Na also correlated with minimal changes to micro-scale preservation of
446 nano-scale porosity (1-100 nm). However, no significant changes in Mg-Al pairing were
447 observed in these samples and, as a result, polyvalent cationic stabilization was not evidenced in
448 these samples.

449 Experimental data also indicate that brucite improves acid resistance in AACs with high
450 alkali (Na:Al = 1.39) contents by increasing acid neutralization capacity *and* polyvalent cationic
451 stabilization. Upon acid exposure, addition of brucite improved acid resistance, as evidenced by
452 lower Al, Si, and Na leaching and simultaneous increases in acid neutralization capacity
453 compared samples without brucite. However, the acid neutralization capacity was dependent on
454 Mg leaching and, during the second acid exposure, Mg was retained within the material's
455 microstructure. This retention led to a decrease in the acid neutralization capacity and a
456 concomitant increase in Mg-Al interactions, as evinced *via* electron microprobe analysis. Results
457 also demonstrate that, while the nano-scale porous structure was preserved in these samples,
458 there was an increase in pore sizes <5nm. Increased nano-scale porosity likely increased the
459 tortuosity and brucite dissolution, which supports the increase in Mg-Al pairing observed.
460 Together, these results provide evidence in support of polyvalent cationic stabilization as a
461 unique acid resistance mechanism that preserves the integrity of aluminosilicate binders upon
462 exposure to acid.

463 **5. References**

- 464 [1] Roy D M, Alkali activated cements, opportunities and challenges, *Cem. Concr. Res.* 29 (1999) 249–
 465 254.
- 466 [2] B. Singh, G. Ishwarya, M. Gupta, S.K. Bhattacharyya, Geopolymer concrete: A review of some
 467 recent developments, *Constr. Build. Mater.* 85 (2015) 78–90.
 468 <https://doi.org/10.1016/J.CONBUILDMAT.2015.03.036>.
- 469 [3] J. Provis, Geopolymers and other alkali activated material: why, how, what? , *Mater. Struct.* 47
 470 (2013) 25.
- 471 [4] L. Struble, E. Kim, L. Gomez-Zamorano, Overview of Geopolymer cement, (2013).
- 472 [5] P. Duxson, a. Fernández-Jiménez, J.L. Provis, G.C. Lukey, a. Palomo, J.S.J. van Deventer,
 473 Geopolymer technology: the current state of the art, *J. Mater. Sci.* 42 (2007) 2917–2933.
 474 <https://doi.org/10.1007/s10853-006-0637-z>.
- 475 [6] J.L. Provis, A. Palomo, C. Shi, Advances in understanding alkali-activated materials, *Cem Concr*
 476 *Res.* 78 (2015) 110–125. <https://doi.org/10.1016/j.cemconres.2015.04.013>.
- 477 [7] A. Fernandez-Jimenez, A. Palomo, Chemical durability of Geopolymers, in: J.L. Provis, J. Van
 478 Deventer (Eds.), *Geopolymers- Struct. Process. Prop. Ind. Appl.*, 2009: pp. 167–193.
- 479 [8] A. Allahverdi, F. Skvara, Acidic corrosion of hydrated cement based materials. Part 1. Mechanism
 480 of the Phenomenon, *Ceram.-Silikáty.* 44 (2000) 152–160.
- 481 [9] T. Bakharev, J.G. Sanjayan, Y.B. Cheng, Resistance of alkali-activated slag concrete to acid attack,
 482 *Cem. Concr. Res.* 33 (2003) 1607–1611. [https://doi.org/10.1016/S0008-8846\(03\)00125-X](https://doi.org/10.1016/S0008-8846(03)00125-X).
- 483 [10] F. Pacheco-Torgal, J. Castro-Gomes, S. Jalali, Alkali-activated binders: A review. Part 1. Historical
 484 background, terminology, reaction mechanisms and hydration products, *Constr. Build. Mater.* 22
 485 (2008) 1305–1314. <https://doi.org/10.1016/j.conbuildmat.2007.10.015>.
- 486 [11] T. Bakharev, Resistance of geopolymer materials to acid attack, *Cem. Concr. Res.* 35 (2005) 658–
 487 670. <https://doi.org/10.1016/j.cemconres.2004.06.005>.
- 488 [12] C. Grengg, F. Mittermayr, N. Ukrainczyk, G. Koraimann, S. Kienesberger, M. Dietzel, Advances in
 489 concrete materials for sewer systems affected by microbial induced concrete corrosion: A review,
 490 *Water Res.* 134 (2018) 341–352. <https://doi.org/10.1016/j.watres.2018.01.043>.
- 491 [13] R.J. Myers, B. Lothenbach, S.A. Bernal, J.L. Provis, Thermodynamic modelling of alkali-activated
 492 slag cements, *Appl. Geochem.* 61 (2015) 233–247.
 493 <https://doi.org/10.1016/J.APGEOCHEM.2015.06.006>.
- 494 [14] C.-L. Hwang, D.-H. Vo, V.-A. Tran, M.D. Yehualaw, Effect of high MgO content on the
 495 performance of alkali-activated fine slag under water and air curing conditions, *Constr. Build.*
 496 *Mater.* 186 (2018) 503–513. <https://doi.org/10.1016/J.CONBUILDMAT.2018.07.129>.
- 497 [15] T. Yang, X. Yao, Z. Zhang, Geopolymer prepared with high-magnesium nickel slag:
 498 Characterization of properties and microstructure, *Constr. Build. Mater.* 59 (2014) 188–194.
 499 <https://doi.org/10.1016/J.CONBUILDMAT.2014.01.038>.
- 500 [16] X. Huang, S. Hu, F. Wang, Y. Liu, Y. Mu, Properties of alkali-activated slag with addition of cation
 501 exchange material, *Constr. Build. Mater.* 146 (2017) 321–328.
 502 <https://doi.org/10.1016/j.conbuildmat.2017.03.127>.
- 503 [17] J.P. Gevaudan, A. Caicedo-Ramirez, M.T. Hernandez, W. V. Srubar, Copper and cobalt improve the
 504 acid resistance of alkali-activated cements, *Cem. Concr. Res.* 115 (2018) 1–12.
 505 <https://doi.org/10.1016/j.cemconres.2018.08.002>.
- 506 [18] T. Yang, Z. Zhang, H. Zhu, X. Gao, C. Dai, Q. Wu, Re-examining the suitability of high
 507 magnesium nickel slag as precursors for alkali-activated materials, *Constr. Build. Mater.* 213 (2019)
 508 109–120. <https://doi.org/10.1016/j.conbuildmat.2019.04.063>.
- 509 [19] M.X. Peng, Z.H. Wang, Q.G. Xiao, F. Song, W. Xie, L.C. Yu, H.W. Huang, S.J. Yi, Effects of
 510 alkali on one-part alkali-activated cement synthesized by calcining bentonite with dolomite and
 511 Na₂CO₃, *Appl. Clay Sci.* 139 (2017) 64–71. <https://doi.org/10.1016/j.clay.2017.01.020>.

- 512 [20] R.J. Myers, S.A. Bernal, J.L. Provis, Phase diagrams for alkali-activated slag binders, *Cem. Concr.*
513 *Res.* 95 (2017) 30–38. <https://doi.org/10.1016/j.cemconres.2017.02.006>.
- 514 [21] J.P. Gevaudan, K.M. Campbell, T.J. Kane, R.K. Shoemaker, W. V. Srubar, Mineralization
515 dynamics of metakaolin-based alkali-activated cements, *Cem. Concr. Res.* 94 (2017) 1–12.
516 <https://doi.org/10.1016/j.cemconres.2017.01.001>.
- 517 [22] X. Gao, Q.L. Yu, H.J.H. Brouwers, Assessing the porosity and shrinkage of alkali activated slag-fly
518 ash composites designed applying a packing model, *Constr. Build. Mater.* 119 (2016) 175–184.
519 <https://doi.org/10.1016/j.conbuildmat.2016.05.026>.
- 520 [23] D. Nied, K. Enemark-rasmussen, E.L. Hopital, J. Skibsted, B. Lothenbach, Properties of magnesium
521 silicate hydrates (M-S-H), *Cem. Concr. Res.* 79 (2016) 323–332.
- 522 [24] P. Duxson, G.C. Lukey, F. Separovic, J.S.J. Van Deventer, Effect of Alkali Cations on Aluminum
523 Incorporation in Geopolymeric Gels, (2005) 832–839.
- 524 [25] X. Chen, A. Sutrisno, L. Zhu, L.J. Struble, Setting and nanostructural evolution of metakaolin
525 geopolymer, *J. Am. Ceram. Soc.* 100 (2017) 2285–2295.
- 526 [26] F. Pacheco-Torgal, Z. Abdollahnejad, a. F. Camões, M. Jamshidi, Y. Ding, Durability of alkali-
527 activated binders: A clear advantage over Portland cement or an unproven issue?, *Constr. Build.*
528 *Mater.* 30 (2012) 400–405. <https://doi.org/10.1016/j.conbuildmat.2011.12.017>.
- 529 [27] O. Burciaga-Díaz, J.I. Escalante-García, Strength and Durability in Acid Media of Alkali Silicate-
530 Activated Metakaolin Geopolymers, *J. Am. Ceram. Soc.* 95 (2012) 2307–2313.
531 <https://doi.org/10.1111/j.1551-2916.2012.05249.x>.
- 532 [28] A. Palomo, M.T.T. Blanco-Varela, M.L.L. Granizo, F. Puertas, T. Vazquez, M.W.W. Grutzeck,
533 Chemical stability of cementitious materials based on metakaolin, *Cem. Concr. Res.* 29 (1999) 997–
534 1004. [https://doi.org/10.1016/S0008-8846\(99\)00074-5](https://doi.org/10.1016/S0008-8846(99)00074-5).
- 535 [29] C. Grengg, N. Ukrainczyk, G. Koraimann, B. Mueller, M. Dietzel, F. Mittermayr, Long-term in situ
536 performance of geopolymer, calcium aluminate and Portland cement-based materials exposed to
537 microbially induced acid corrosion, *Cem. Concr. Res.* 131 (2020) 106034.
538 <https://doi.org/10.1016/j.cemconres.2020.106034>.
- 539 [30] P. Sturm, G.J.G. Gluth, C. Jäger, H.J.H. Brouwers, H.-C. Kühne, Sulfuric acid resistance of one-part
540 alkali-activated mortars, *Cem. Concr. Res.* 109 (2018) 54–63.
541 <https://doi.org/10.1016/j.cemconres.2018.04.009>.
- 542 [31] F.F. Škvára, V.V. Šmilauer, P. Hlaváček, L. Kopecký, Z. Cílová, P. Hlaváček, L. Kopecky, Z.
543 Cílová, A Weak Alkali Bond in (N,K)-A-S-H Gels: Evidence from Leaching and Modeling, *Ceram.*
544 *– Silikáty.* 56 (2012) 374–382.
- 545 [32] P.-T. Fernando, J. Said, Resistance to acid attack, abrasion and leaching behavior of alkali-activated
546 mine waste binders, *Mater. Struct.* 44 (2011) 487–498. <https://doi.org/10.1617/s11527-010-9643-3>.
- 547 [33] M. Mustafa Al Bakri Abdullah, H. Kamarudin, A. Victor Sandu Gheorghe Asachi, C. Mohd
548 Ruzaidi, M. Al Bakri Abdullah, Sulfuric Acid Attack on Ordinary Portland Cement and
549 Geopolymer Material, n.d.
- 550 [34] O.S. Pokrovsky, J. Schott, Experimental study of brucite dissolution and precipitation in aqueous
551 solutions: surface speciation and chemical affinity control, *Geochim. Cosmochim. Acta.* 68 (2004)
552 31–45. [https://doi.org/10.1016/S0016-7037\(03\)00238-2](https://doi.org/10.1016/S0016-7037(03)00238-2).
- 553 [35] J.W. Johnson, E.H. Oelkers, H.C. Helgeson, SUPCRT92: A software package for calculating the
554 standard molal thermodynamic properties of minerals, gases, aqueous species, and reactions from 1
555 to 5000 bar and 0 to 1000°C, *Comput. Geosci.* 18 (1992) 899–947. [https://doi.org/10.1016/0098-3004\(92\)90029-Q](https://doi.org/10.1016/0098-3004(92)90029-Q).
- 556 [36] E.H. Oelkers, P. Benezeth, G.S. Pokrovski, Thermodynamic Databases for Water-Rock Interaction,
557 *Rev. Mineral. Geochem.* 70 (2009) 1–46. <https://doi.org/10.2138/rmg.2009.70.1>.
- 558 [37] J.L. Provis, R.J. Myers, C.E. White, V. Rose, J.S.J.J. Van Deventer, X-ray microtomography shows
559 pore structure and tortuosity in alkali-activated binders, *Cem. Concr. Res.* 42 (2012) 855–864.
560 <https://doi.org/10.1016/j.cemconres.2012.03.004>.
- 561

- 562 [38] S. Das, P. Yang, S.S. Singh, J.C.E. Mertens, X. Xiao, N. Chawla, N. Neithalath, Effective properties
563 of a fly ash geopolymer: Synergistic application of X-ray synchrotron tomography, nanoindentation,
564 and homogenization models, *Cem. Concr. Res.* 78 (2015) 252–262.
565 <https://doi.org/10.1016/J.CEMCONRES.2015.08.004>.
- 566 [39] D. Ravikumar, S. Peethamparan, N. Neithalath, Structure and strength of NaOH activated concretes
567 containing fly ash or GGBFS as the sole binder, *Cem. Concr. Compos.* 32 (2010) 399–410.
568 <https://doi.org/10.1016/J.CEMCONCOMP.2010.03.007>.
- 569 [40] D.W. Law, A.A. Adam, T.K. Molyneaux, I. Patnaikuni, Durability assessment of alkali activated
570 slag (AAS) concrete, *Mater. Struct.* 45 (2012) 1425–1437. [https://doi.org/10.1617/s11527-012-](https://doi.org/10.1617/s11527-012-9842-1)
571 [9842-1](https://doi.org/10.1617/s11527-012-9842-1).
- 572 [41] A. Favier, J. Hot, G. Habert, N. Roussel, J.-B. d’Espinose de Lacaillerie, Flow properties of MK-
573 based geopolymer pastes. A comparative study with standard Portland cement pastes, *Soft Matter.*
574 10 (2014) 1134–1141.
- 575 [42] P. Chindaprasirt, T. Chareerat, V. Sirivivatnanon, Workability and strength of coarse high calcium
576 fly ash geopolymer, *Cem. Concr. Compos.* 29 (2007) 224–229.
577 <https://doi.org/10.1016/j.cemconcomp.2006.11.002>.
- 578 [43] K.L. Aughenbaugh, T. Williamson, M.C.G. Juenger, Critical evaluation of strength prediction
579 methods for alkali-activated fly ash, *Mater. Struct.* 48 (2015) 607–620.
580 <https://doi.org/10.1617/s11527-014-0496-z>.
- 581 [44] Y.M. Liew, H. Kamarudin, A.M. Mustafa Al Bakri, M. Bnhussain, M. Luqman, I. Khairul Nizar,
582 C.M. Ruzaidi, C.Y. Heah, Optimization of solids-to-liquid and alkali activator ratios of calcined
583 kaolin geopolymeric powder, *Constr. Build. Mater.* 37 (2012) 440–451.
584 <https://doi.org/10.1016/J.CONBUILDMAT.2012.07.075>.
- 585 [45] P.S. Das, M. Bhattacharya, D.K. Chanda, S. Dalui, S. Acharya, S. Ghosh, A.K. Mukhopadhyay,
586 Failure and deformation mechanisms at macro- and nano-scales of alkali activated clay, *J. Phys.*
587 *Appl. Phys.* 49 (2016) 235503. <https://doi.org/10.1088/0022-3727/49/23/235503>.
- 588 [46] N.R. Rakhimova, R.Z. Rakhimov, Reaction products, structure and properties of alkali-activated
589 metakaolin cements incorporated with supplementary materials – a review, *J. Mater. Res. Technol.*
590 (2018). <https://doi.org/10.1016/J.JMRT.2018.07.006>.
- 591